Characterization of Ultrathin Fe–Co Layer Grown on Amorphous Co–Fe–B by In situ Reflective High-Energy Electron Diffraction

2013 Appl. Phys. Express 6 063003

(http://iopscience.iop.org/1882-0786/6/6/063003)

Applied Physics Express 6 (2013) 063003
http://dx.doi.org/10.7567/APEX.6.063003

Characterization of Ultrathin Fe–Co Layer Grown on Amorphous Co–Fe–B by In situ Reflective High-Energy Electron Diffraction

Hiroyuki Hosoya[1,3], Yoshinori Nagamine[1,3], Koji Tsunekawa[1,3], Vadym Zayets[2], and Shinji Yuasa[2,3*]

[1]*Process Development Center, Canon ANELVA Corporation, Kawasaki 215-8550, Japan*
[2]*National Institute of Advanced Industrial Science and Technology (AIST), Spintronics Research Center, Tsukuba, Ibaraki 305-8568, Japan*
[3]*CREST, Japan Science and Technology Agency (JST), Kawaguchi, Saitama 332-0012, Japan*
E-mail: yuasa-s@aist.go.jp

Received April 8, 2013; accepted May 8, 2013; published online May 23, 2013

The textured MgO(001) tunnel barrier grown on CoFeB is a fundamental building block for spintronic devices such as magnetic tunnel junctions. Although the insertion of an ultrathin Fe–Co layer between an MgO layer and a bottom CoFeB layer is a common technique for improving the magnetoresistance effect, the characteristics of this technique remain unclear. We systematically investigated the as-grown structure of Fe–Co by reflective high-energy electron diffraction and found that a highly textured MgO(001) is formed only on an amorphous Fe–Co surface. The diffusion of B atoms from underlying CoFeB into Fe–Co is what makes the as-grown Fe–Co layer amorphous.

MgO-based magnetic tunnel junctions (MTJs) with a (001)-oriented single-crystalline or polycrystalline (textured) MgO tunnel barrier exhibit a giant tunnel magnetoresistance (TMR) effect with magnetoresistance (MR) ratios of up to a few hundred percent at room temperature (RT).[1–3] MTJs with a CoFeB/MgO/CoFeB structure are especially useful for practical applications such as magnetic sensors and spin-transfer-torque magnetoresistive random access memory (STT-MRAM) due to their compatibility with mass-manufacturing processes.[4] In CoFeB/MgO/CoFeB MTJs, the CoFeB bottom electrode layer is first formed as an amorphous phase and then a textured MgO(001) barrier layer is grown on the amorphous CoFeB surface at room temperature, usually by sputtering deposition. By post-annealing the CoFeB/MgO/CoFeB structure, the CoFeB electrode layers can be crystallized from the interfaces with the MgO(001) layer due to solid-phase epitaxial growth.[5,6] As a result, the MTJ structure becomes textured bcc CoFeB(001)/MgO(001)/bcc CoFeB(001), which is essential for the giant MR ratios.

The basic CoFeB/MgO/CoFeB structure is often modified, for example, by inserting an ultrathin Fe–Co layer between the MgO and CoFeB layers to further optimize the magneto-transport properties.[7–10] In our previous study,[8] we fabricated perpendicularly magnetized MTJs with the bottom electrode structure of CoPt/$Co_{60}Fe_{20}B_{20}$ (1 nm)/$Fe_{30}Co_{70}$ (0.3 nm). Without the 0.3-nm-thick insertion layer, we observed a significant reduction in the MR ratio. Schreiber et al.[9] observed an increase in the MR ratio from 105 to 192% by inserting a 1.5-nm-thick $Fe_{10}Co_{90}$ layer between the bottom CoFeB electrode and MgO barrier layers. Yoshida et al.[10] observed a similar increase in the MR ratio by inserting a 0.4-nm-thick $Fe_{50}Co_{50}$ layer between the bottom CoFeB electrode and MgO barrier layers. The insertion of an ultrathin Fe–Co layer often improves the MR ratio, especially in an ultralow resistance–area (*RA*) product region and/or when the post-annealing temperature is relatively low (~250 °C) although the detailed mechanism has been unclear. Note that the high MR ratio with ultra-low *RA* product is important for both high-density STT-MRAM and read heads of hard disk drives (HDDs), and the low annealing temperature is important for the HDD read heads, whose process temperature should be kept below about 250 °C.

To investigate the mechanism of the MR enhancement, Choi et al.[7] investigated the growth and crystallization processes of the CoFeB/Fe–Co/MgO structure by cross-sectional transmission electron microscopy (TEM) and concluded that the Fe–Co layer deposited on an amorphous CoFeB crystallizes in the bcc(001) textured structure in the as-grown state and acts as a template to crystallize the MgO layer in a highly (001)-oriented texture. This claim is, however, contradictory to previous works reporting that a highly oriented MgO(001) layer can be grown on an amorphous CoFeB surface.[4–6] Although the insertion of an ultrathin Fe–Co layer is a commonly used technique both in basic research and device application, there have been no systematic reports on the structure and functions of the insertion layer. In this study, we systematically investigated the growth and crystallization processes of the CoFeB/Fe–Co/MgO structure by in situ reflective electron diffraction (RHEED) and obtained a phase diagram of the as-grown Fe–Co layer with respect to the thickness and chemical composition. We also investigated the diffusion of B atoms from the underlying CoFeB into the Fe–Co layer.

The thin films were deposited on thermally oxidized Si(001) wafers of 200 mm diameter using a magnetron-sputtering system (Canon ANELVA C-7100) developed for the mass production of HDD read heads and MRAM. The stacking structure of the samples is shown in Fig. 1. We used standard techniques and conditions for preparing the CoFeB/MgO/CoFeB MTJ films[4,11–13] and deposited a 30-Å-thick $Co_{60}Fe_{20}B_{20}$ layer that corresponds to the bottom ferromagnetic electrode of MTJ onto a thermally oxidized Si substrate with a Ta seed layer. On the CoFeB layer, we deposited a Fe–Co alloy layer with various thicknesses (0 to 30 Å) and chemical compositions (from $Fe_{90}Co_{10}$ to $Fe_{10}Co_{90}$) at RT. Then, a 10-Å-thick MgO layer, which corresponds to the tunnel barrier of the MTJ, was deposited at RT by rf sputtering from an MgO target under practical conditions for achieving giant MR ratios.[12] We performed in situ RHEED observation to characterize the structure of each layer (see Fig. 1). A special RHEED observation chamber was attached to our manufacturing-type sputtering system for the in situ RHEED observations. In situ RHEED is an ideal technique to observe the as-grown surface structure of ultrathin layers. Note that in the cross-sectional TEM observations, the processes to prepare the TEM

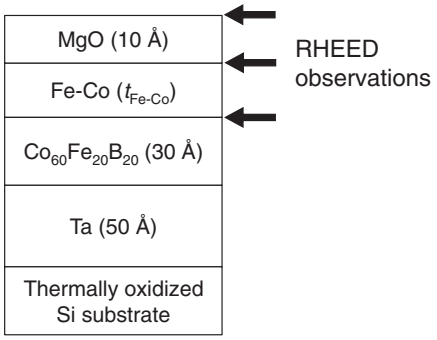

Fig. 1. Schematic stacking structure of samples for in situ RHEED observations. RHEED images were observed at growth steps indicated by arrows.

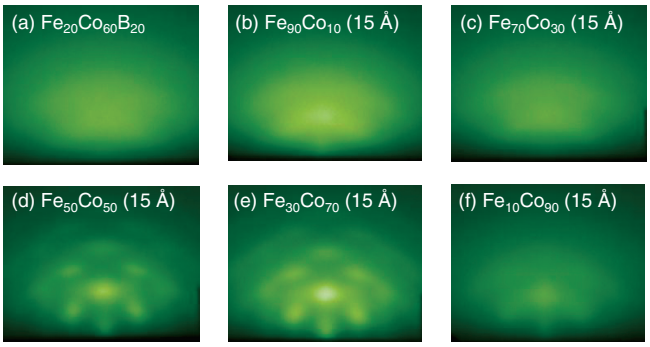

Fig. 2. (a) In situ RHEED image of 30-Å-thick $Co_{60}Fe_{20}B_{20}$ layer. (b)–(f) In situ RHEED images of 15-Å-thick Fe–Co layers grown on $Co_{60}Fe_{20}B_{20}$ layer. Compositions of Fe–Co are (b) $Fe_{90}Co_{10}$, (c) $Fe_{70}Co_{30}$, (d) $Fe_{50}Co_{50}$, (e) $Fe_{30}Co_{70}$, and (f) $Fe_{10}Co_{90}$.

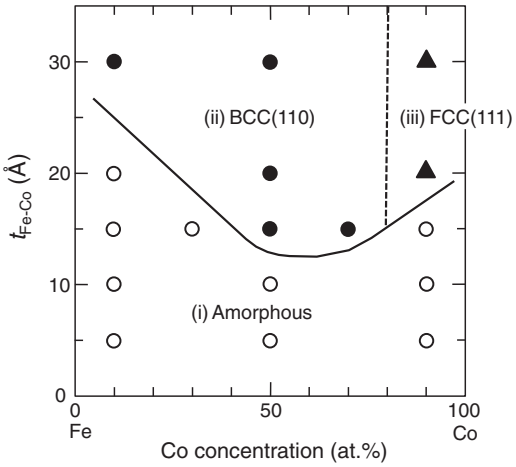

Fig. 3. As-grown structure of Fe–Co layer on amorphous $Co_{60}Fe_{20}B_{20}$. Fe–Co layer is amorphous in area (i), bcc(110)-oriented polycrystalline in area (ii), and fcc(111)-oriented polycrystalline in area (iii).

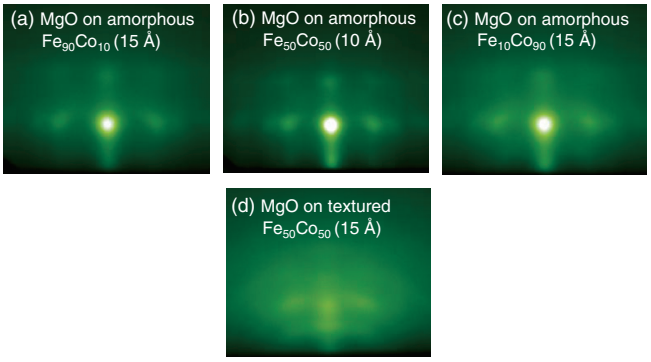

Fig. 4. In situ RHEED images 10-Å-thick MgO layers grown on various Fe–Co underlayers. The underlayers are (a) amorphous $Fe_{90}Co_{10}$ (15 Å), (b) amorphous $Fe_{50}Co_{50}$ (10 Å), (c) amorphous $Fe_{10}Co_{90}$ (15 Å), and (d) bcc(110)-oriented polycrystalline $Fe_{50}Co_{50}$ (15 Å).

samples (ion milling, etc.) might damage the samples and change the structure from the as-grown one.

The RHEED image of the as-grown CoFeB surface is shown in Fig. 2(a). The CoFeB layer has an amorphous structure in the as-grown state, as observed in previous works.[5,6] Figures 2(b)–2(f) are the RHEED images of 15-Å-thick Fe–Co layers with various compositions. While the $Fe_{50}Co_{50}$ and $Fe_{30}C_{70}$ layers showed clear diffraction patterns, which represent the bcc(110) textured structure, the Fe–Co layers with Fe-rich ($Fe_{90}Co_{10}$, $Fe_{70}Co_{30}$) and Co-rich ($Fe_{10}Co_{90}$) compositions showed a halo pattern with no clear diffraction spots, which indicates an amorphous structure. Figure 3 shows a summary of the structure of the as-grown Fe–Co layers with various thicknesses and compositions. In the entire composition range, Fe–Co is amorphous for $t_{Fe-Co} \leq 10$ Å. Fe–Co becomes crystalline above a certain critical thickness, which largely depends on the composition of Fe–Co. Above the critical thickness, Fe–Co has a textured bcc(110) structure for Co concentration $\leq$70 at. % and a textured fcc(111) structure for Co concentration of 90 at. %. It should be noted that both bcc(110) and fcc(111) are energetically stable crystallographic planes with a close-packing structure. It is therefore natural to have these textured structures in relatively thick Fe–Co layers facing a vacuum surface. This result contradicts the study by Choi et al., in which they report the formation of a textured bcc(001) Fe–Co layer on amorphous CoFeB in the as-grown state.[7] Because Choi et al. used ex situ cross-sectional TEM observations for the structural analysis, the Fe–Co layer might have crystallized in the bcc(001) structure during the preparation processes for the TEM samples.

Figures 4(a)–4(d) are the RHEED images for the 10-Å-thick MgO layers grown on Fe–Co layers with various thicknesses and compositions. In Figs. 4(a)–4(c), the MgO layers were grown on the amorphous surfaces of $Fe_{90}Co_{10}$, $Fe_{50}Co_{50}$, and $Fe_{10}Co_{90}$. In these cases, highly (001)-oriented polycrystalline MgO layers were grown, as seen in the figures. In contrast, in Fig. 4(d), the MgO layer grown on the bcc(110)-oriented polycrystalline Fe–Co layer showed poor crystallinity: its RHEED pattern is faint and broad, indicating a very poor (001) orientation of MgO. This is probably due to the poor in-plane lattice matching between the bcc Fe–Co(110) and MgO(001) layers. These results clearly indicate that the highly textured MgO(001) layer is formed only on the amorphous surface of Fe–Co–(B). Crystallization of the Fe–Co surface in the as-grown state results in the degradation of the (001) orientation of MgO. The phase diagram in Fig. 3 therefore provides us with invaluable information for achieving giant MR ratios in MgO-based MTJs.

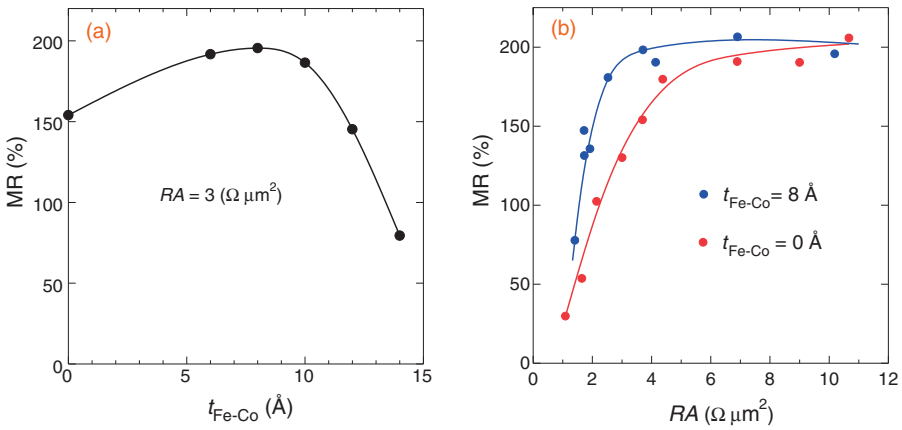

Fig. 5. MR ratio at room temperature for $Co_{60}Fe_{20}Co_{20}/Fe_{30}Co_{70}/MgO/Co_{60}Fe_{20}B_{20}$ magnetic tunnel junctions. (a) Dependence of MR ratio on thickness of $Fe_{30}Co_{70}$ layer (t_{Fe-Co}). (b) Dependence of MR ratio on RA product for MTJs with $t_{FeCo} = 0$ and 8 Å.

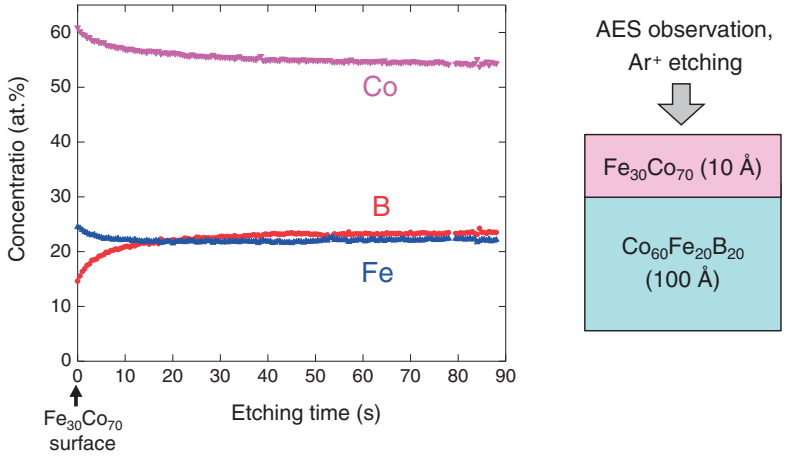

Fig. 6. Depth profile of film composition investigated by AES for $Co_{60}Fe_{20}B_{20}$ (10 Å)/$Fe_{30}Co_{70}$ (10 Å) bilayer structure. AES was observed while etching the film by Ar-ion milling. Zero etching time corresponds to the surface of 10-Å-thick $Fe_{30}Co_{70}$.

The relation between the MR ratio and the growth and crystallization processes of the Fe–Co insertion layer is discussed below. We fabricated MTJs with $Co_{60}Fe_{20}B_{20}$/Fe–Co/MgO/$Co_{60}Fe_{20}B_{20}$ structure by varying the thickness and composition of Fe–Co and measured the magneto-transport properties. Figure 5(a) shows the t_{Fe-Co} dependence of the MR ratio for the MTJs with $Fe_{30}Co_{70}$ insertion layer. The insertion of the Fe–Co layer initially increased the MR ratio, as observed in previous studies. For $t_{Fe-Co} > 1$ nm, a large reduction in the MR ratio was observed. This behavior is well explained by the phase diagram (Fig. 3). For $t_{Fe-Co} > 1$ nm, the as-grown $Fe_{30}Co_{70}$ layer has bcc(110) structure, on which a high-quality MgO(001) cannot be grown. The behaviors observed in previous studies[9,10] also match with the phase diagram. Figure 5(b) shows the RA dependence of MR ratio for MTJs with $t_{FeCo} = 0$ and 8 Å. The Fe–Co insertion is effective for improving the MR ratio when the RA product is below several Ω μm^2, which is the important area for both the STT-MRAM and HDD read head applications.

It is important to clarify why the Fe–Co layer has an amorphous structure below the critical thickness. One possible explanation is the underlying amorphous CoFeB layer, which acts as a template to make the Fe–Co layer amorphous. However, an amorphous underlying layer does not always make the ultrathin Fe–Co layer amorphous. When a 10-Å-thick Fe–Co layer was deposited on an amorphous SiO_2 layer, for example, the Fe–Co layer was polycrystalline even in the as-grown state. Another possible explanation is the diffusion of B atoms from CoFeB into Fe–Co, which will stabilize the amorphous Fe–Co. To test this hypothesis, we carried out an in situ Auger electron spectroscopy (AES) observation. We deposited a 10-Å-thick $Fe_{30}Co_{70}$ layer on an amorphous $Co_{60}Fe_{20}B_{20}$ layer (see Fig. 6) and then observed the surface composition by AES while etching the film from the surface by Ar-ion milling. The observed depth profile of the film composition is shown in Fig. 6. Here, zero etching time corresponds to the initial surface of the 10-Å-thick $Fe_{30}Co_{70}$ layer. A certain number of B atoms were clearly detected even when the CoFeB was covered by the 10-Å-thick $Fe_{30}Co_{70}$ layer. Here, we should discuss the effect of the penetration of Auger electrons through the Fe–Co layer, since some of the Auger electrons could have originated from the underlying CoFeB layer. According to previous research,[14] the attenuation length of Auger electrons in 3d transition metals is about 4 Å at the energy of 200 eV, which corresponds to the energy of Auger electrons from B atoms. Because the thickness of the Fe–Co layer (10 Å) is more than twice the attenuation length (4 Å), most of the Auger electrons from the B atoms in the

underlying CoFeB should be absorbed in the Fe–Co layer and cannot be emitted from the Fe–Co surface. Therefore, the large B signal detected in Fig. 6 at zero etching time indicates that a certain number of B atoms diffused from the underlying CoFeB layer into the Fe–Co layer even in the as-grown state, which made the as-grown Fe–Co layer amorphous. The Fe–Co insertion layer is actually a nano-scale "graded" material made of Fe, Co, and B, in which the B concentration is smaller (but not zero) at the interface with MgO. The smaller B concentration near the Fe–Co(B)/MgO interface promotes the solid-phase epitaxial growth from the interface by lowering the crystallization temperature from the MgO interface during post-annealing, thus improving the bcc(001) orientation in the Fe–Co(B) layer. This is considered to be the mechanism for the improvement of the MR ratio in previous studies.[7–10)]

In conclusion, we studied the growth of a CoFeB/Fe–Co/MgO structure by in situ RHEED observation and obtained a phase diagram of the as-grown Fe–Co layer. Below the critical thickness of the Fe–Co layer, Fe–Co becomes amorphous in the as-grown state. A highly oriented MgO(001) layer is grown only on the amorphous Fe–Co surface. AES observation revealed that B atoms diffuse from the underlying CoFeB into Fe–Co layers, which is what makes the Fe–Co layer amorphous in the as-grown state. These results provide us with invaluable information for achieving giant MR ratios in MgO-based MTJs.

Acknowledgment We are grateful to Dr. Yoshishige Suzuki of Osaka University for helpful discussion on AES.

1) S. Yuasa, A. Fukushima, T. Nagahama, K. Ando, and Y. Suzuki: Jpn. J. Appl. Phys. **43** (2004) L588.
2) S. S. P. Parkin, C. Kaiser, A. Panchula, P. M. Rice, B. Hughes, M. Samant, and S.-H. Yang: Nat. Mater. **3** (2004) 862.
3) S. Yuasa, T. Nagahama, A. Fukushima, Y. Suzuki, and K. Ando: Nat. Mater. **3** (2004) 868.
4) D. D. Djayaprawira, K. Tsunekawa, M. Nagai, H. Maehara, S. Yamagata, N. Watanabe, S. Yuasa, Y. Suzuki, and K. Ando: Appl. Phys. Lett. **86** (2005) 092502.
5) S. Yuasa, Y. Suzuki, T. Katayama, and K. Ando: Appl. Phys. Lett. **87** (2005) 242503.
6) S. Yuasa and D. D. Djayaprawira: J. Phys. D **40** (2007) R337.
7) Y.-S. Choi, H. Tsunematsu, S. Yamagata, H. Okuyama, Y. Nagamine, and K. Tsunekawa: Jpn. J. Appl. Phys. **48** (2009) 120214.
8) K. Yakushiji, K. Noma, T. Saruya, H. Kubota, A. Fukushima, T. Nagahama, S. Yuasa, and K. Ando: Appl. Phys. Express **3** (2010) 053003.
9) D. K. Schreiber, Y.-S. Choi, Y. Lin, A. N. Chiaramonti, D. N. Seidman, and A. K. Petford-Long: Appl. Phys. Lett. **98** (2011) 232506.
10) C. Yoshida, T. Ochiai, and T. Sugii: J. Appl. Phys. **111** (2012) 07C716.
11) K. Tsunekawa, D. D. Djayaprawira, M. Nagai, H. Maehara, S. Yamagata, N. Watanabe, S. Yuasa, Y. Suzuki, and K. Ando: Appl. Phys. Lett. **87** (2005) 072503.
12) Y. Nagamine, H. Maehara, K. Tsunekawa, D. D. Djayaprawira, N. Watanabe, S. Yuasa, and K. Ando: Appl. Phys. Lett. **89** (2006) 162507.
13) H. Maehara, K. Nishimura, Y. Nagamine, K. Tsunekawa, T. Seki, H. Kubota, A. Fukushima, K. Yakushiji, K. Ando, and S. Yuasa: Appl. Phys. Express **4** (2011) 033002.
14) P. J. Cumpson and M. P. Seah: Surf. Interface Anal. **25** (1997) 430.